Biosensors and Bioelectronics 142 (2019) 111546

Contents lists available at ScienceDirect

Biosensors and Bioelectronics

journal homepage: www.elsevier.com/locate/bios

Enhanced photoelectric conversion efficiency: A novel h-BN based self-powered photoelectrochemical aptasensor for ultrasensitive detection of diazinon

Jisui Tan[a,b], Bo Peng[a,b], Lin Tang[a,b,*], Chengyang Feng[a,b], Jiajia Wang[a,b], Jiangfang Yu[a,b], Xilian Ouyang[a,b], Xu Zhu[a,b]

[a] College of Environmental Science and Engineering, Hunan University, Changsha, 410082, China
[b] Key Laboratory of Environmental Biology and Pollution Control (Hunan University), Ministry of Education, Changsha, 410082, Hunan, China

ARTICLE INFO

Keywords:
Hexagonal boron nitride
Self-powered
Photoelectrochemical aptasensor
Photoelectric conversion efficiency
Diazinon

ABSTRACT

This work presents a novel hexagonal boron nitride (h-BN) based self-powered photoelectrochemical (PEC) aptasensor for ultrasensitive detection of diazinon (DZN) with excellent photoelectric conversion efficiency. It was the first time that h-BN based materials were applied to PEC aptasensor, in which the construction of Z-scheme heterojunction of h-BN and graphitic carbon nitride (CN) via doping sulfur into h-BN was innovatively proposed. Meanwhile, Au nanoparticles (AuNPs) were utilized for the surface plasmon resonance (SPR) effect and the formation of new recombination centers. The charge transfer mechanism was expounded and verified by the electron spin resonance (ESR) spin-trap technique. The proposed PEC aptasensor for determination of DZN exhibited a wide linear range from 0.01 to 10000 nM and a low detection limit of 6.8 pM with superb selectivity and remarkable stability. Moreover, the constructed PEC aptasensor performed well with excellent recoveries in three different real samples. This work illustrated that PEC aptasensor is a promising alternative to conventional analytical technologies for the detection of DZN and other organophosphorus (OP) pesticides. The designing ideas of the proposed h-BN based material can provide a foothold for the innovative construction of photoactive materials for PEC bioanalysis.

1. Introduction

Rapid, sensitive, and stabile bioanalytical technique is significant and indispensable in analytical chemistry and biomolecule research (Li et al., 2017). Photoelectrochemical (PEC) aptasensor as a newly emerged bioanalytical techniques, has attracted considerable attention because of prominent advantages, such as fast response, low background, high sensitivity, simple operation and straightforward detection mechanism (Wang et al., 2019; Zhao et al., 2014). Furthermore, self-powered PEC aptasensor as a brilliant sensing strategy by utilizing excellent photoelectric conversion efficiency without the requirement of external power, has gradually attracted widespread attention (Kang et al., 2015b). And the self-powered ability is benefited from various excellent photoactive materials, such as rGO/ZnO nanorods array (Kang et al., 2015a), NiO/PbS QDs nanostructure (Dai et al., 2017), MoSx@ZnO nanorods array (Shang et al., 2019) and CdS/rGO/ZnO heterostructure (Zhao et al., 2016). Meanwhile, the photocurrent signal of photoactive materials has a great influence on the sensitivity and stability of PEC sensors (Hu et al., 2018; Zheng et al., 2016). Therefore, the excellent photoactive materials with high photoelectric conversion efficiency play an important role in the construction of self-powered PEC aptasensor.

Hexagonal boron nitride (h-BN) is a typical two-dimensional (2D) semiconductor similar to graphene with carbon atoms being replaced by boron and nitrogen (Deepak et al., 2002; Hattori et al., 2014). h-BN based materials have been widely used in durable high-temperature crucibles, protective coatings and photocatalysis field due to their excellent chemical, thermoelectric (Pakdel et al., 2014) and optical properties (Watanabe et al., 2004). Similarly, it has a potential application in PEC aptasensor with superior photoelectric conversion efficiency, environment-friendly property and highly specific surface areas (Lei et al., 2016). However, h-BN can only be excited under ultraviolet radiation due to its large bandgap, which enormously restricts the utilization of visible light (Golberg et al., 2010). Inspiringly, element doping has been an important method to improve the absorption of visible light and narrow the bandgap of photoactive materials (Jiang

* Corresponding author. College of Environmental Science and Engineering, Hunan University, Changsha, 410082, China.
E-mail address: tanglin@hnu.edu.cn (L. Tang).

https://doi.org/10.1016/j.bios.2019.111546
Received 19 June 2019; Received in revised form 24 July 2019; Accepted 27 July 2019
Available online 31 July 2019
0956-5663/

et al., 2017). Especially, doping sulfur heteroatoms into photoactive materials shows prominent enhancement on visible light absorption (He et al., 2015; Liu et al., 2010). Hence, it is necessary for doping heteroatom to enhance the photoelectric response of h-BN under visible-light irradiation. Meanwhile, as a familiar strategy, heterojunction system is introduced to facilitate the effective separation of photogenerated carriers due to the transfer between two semiconductors (Huang et al., 2016; Li et al., 2016). h-BN based heterojunctions exhibit excellent photoelectric activity and have extensive application, such as h-BN nanosheets/TiO_2 (Weng et al., 2015), h-BN/WO_3 (Xu et al., 2016), h-BN/Bi_2WO_6 (Li et al., 2015b), and h-BN/BiOBr (Di et al., 2016). However, compared with typical heterojunction, the Z-scheme heterojunction whose electron-hole transfer pathway has a startling likeness to the letter "Z" (Tang et al., 2018a), can not only possess remarkable reducibility and oxidizability, but also inhibit the recombination of electron-hole pairs (Zhou et al., 2014). Consequently, the Z-scheme heterojunction is a promising strategy to improve the application of h-BN based materials. Graphitic carbon nitride (CN), as a popular photoactive material with nontoxicity, excellent chemical stability and proper bandgap (Wang et al., 2018), has been extensively applied in heterojunctions with other materials (Deng et al., 2018). But CN could hardly couple with h-BN to construct Z-scheme heterojunction owning to the too-large bandgap of pure h-BN for energy band match. Therefore, it is potential for the combination of two strategies (including element doping and Z-scheme heterojunction) to construct a novel h-BN based materials with enhanced photoelectric conversion efficiency. In addition, Au nanoparticles (AuNPs) can promote the transfer of photogenerated carriers and enhance the absorption of visible light due to surface plasmon resonance (SPR) effect. Meanwhile, AuNPs can be able to band with thiol modified aptamer through self-assembly formation of thiol-gold bonding (Au–S). Thus, AuNPs were used to further enhance photoelectric conversion efficiency of the proposed h-BN based photoactive material, and connect with aptamer for the construction of h-BN based self-powered PEC aptasensor.

Organophosphorus (OP) pesticides, as an effective insecticide with high durability, are widely used in agriculture (Tang et al., 2018b). However, a little amount of organophosphorus pesticide residues in water and food can irreversibly inhibit acetylcholine esterase (AChE) and accumulate acetylcholine neurotransmitter leading to neurotoxicity symptom even death (Wang et al., 2013b). Therefore, to detect the concentrations of OP pesticides in environmental samples for public security is still of great necessity and urgency. Diazinon (DZN) as a typical organophosphorus pesticide, has high insecticidal efficiency. Nevertheless, trace residues of DZN in the environment may impair human and animal health. The accepted maximum residue limits (MRLs) of DZN in water and vegetables are 0.1 μg/L and 0.04 μg/g, respectively, according to World Health Organization and European Union (Bhattacharjee et al., 2012). Generally, various methods can be applied for DZN detection, such as gas chromatographic-mass spectrometry (GC-MS) (Armstrong et al., 2014), surface enhanced Raman scattering (SERS) (Wang et al., 2010), high performance liquid chromatography (HPLC) (Zhang and Lee, 2013), chemiluminescence techniques (Wu et al., 2011) and electrochemical strategies (Hassani et al., 2018). However, these methods are often expensive, complex, time-consuming, and need laboratory based large instrumentation (Jenkins et al., 2001). Therefore, to develop a convenient and sensitive PEC aptasensor for detection of DZN certainly becomes an appropriate choice.

In this work, we firstly proposed a novel h-BN based self-powered PEC aptasensor for ultrasensitive determination of DZN with excellent photoelectric conversion efficiency. In the proposed h-BN based photoactive material, sulfur doped h-BN (S-BN) possessed porous structure and large specific surface areas, and was coupled with CN due to the reduced bandgap by doping S into h-BN. AuNPs as a bridge, was used to connect h-BN based photoactive material with aptamer in this PEC aptasensor, to improve the visible light absorption and to inhibit the recombination of electron-hole pairs due to the SPR effect and the formation of new recombination centers. Moreover, the mechanism of the h-BN based PEC aptasensor was explained and verified in detail. The applicability of the fabricated PEC aptasensor for DZN detection was tested in three different real samples.

2. Experimental section

2.1. Materials and instruments

The materials, reagents, and instruments used in this study are described in the "Supporting Information" file.

2.2. Preparation of photoactive materials

The porous h-BN nanosheets were prepared by a simple calcination method. Specifically, boric acid (2.0 g) and urea (8.0 g) were dissolved in 50 mL water, which was stirred for 30 min to obtain a clear colorless solution. Then the mixed precursor solution was transferred into a rotary evaporator at 80 °C until water was vaporized. The obtained gel was heated to 900 °C for 5 h with a heating rate of 4 °C/min under nitrogen atmosphere. After cooling to room temperature, the white porous h-BN nanosheets were collected after ground.

The sulfur doped porous h-BN (S-BN) was synthesized by a typical heat-treat process. h-BN powders (2.0 g) and sublimed sulfur (1.0 g) were well-mixed. The prepared precursor was heated to 440 °C for 120 min with a heating rate of 5 °C/min under nitrogen atmosphere. Subsequently, the temperature kept on increasing to 550 °C for another 2 h to remove the extra sulfur. After being cooled to room temperature, the taupe S-BN powders were collected for use after washing with ethanol and water.

The S-BN/CN composite was prepared via an in-situ growth method. Briefly, S-BN (0.2 g) and different weights of melamine were dissolved in 50 mL ethanol. Subsequently, the mixed suspension was stirred at 80 °C to evaporate the ethanol, and then the resultant powders were heated to 550 °C for 4 h under a heating rate of 3 °C/min. The ultimately obtained yellow powders were denoted as X-S-BN/CN, where X (5, 10, 15, 20, 25) was the mass ratio of melamine to S-BN. For comparison, the pure CN was synthesized without S-BN.

Then the S-BN/Au/CN composite was synthesized through a photoreduction method (Peng et al., 2018). Typically, 50 mg of the above synthesized S-BN/CN powders were dispersed into 30 mL of methanol/water solution (1:5 in volume) for 2 h. Next, suitable amount of $HAuCl_4{\cdot}4H_2O$ solution (1 wt% in water) (the detailed volume was exhibited in Table S1) was dropped in the mixture solution under continuous stirring for 1 h in dark for uniform distribution, and then exposed to a 300 W xenon arc lamp for 1 h. Finally, the obtained product was washed with ethanol and water, and dried at 60 °C. The same method was used to fabricate the S-BN/Au/CN composites with different Au wt% (0.5, 1, 2, 5, 10, 20%).

2.3. Construction of PEC aptasensor

Prior to preparation, the fluorine-doped tin oxide (FTO) glass (1.0 cm × 2.0 cm) was cleaned by successive ultrasonication in acetone, ethanol and water for 10 min, respectively, and dried at 60 °C. Following that, 0.2 mL of S-BN/Au/CN suspension (4.0 mg mL^{-1}; dispersed in 1.0 mL of ethanol and 0.05% Nafion mixture solution) was dropped on the cleaned FTO electrode and dried at room temperature, and marked as S-BN/Au/CN/FTO. Subsequently, 20 μL of 2.5 μM thiolated DZN aptamer stock solution was dropped on the S-BN/Au/CN/FTO surface and incubated at 4 °C for 12 h, and then it spontaneously formed self-assembly monolayer (SAM) through the formation of Au–S bond, marked as aptamer/S-BN/Au/CN/FTO. After the incubation, the modified electrode rinsed with washing buffer solution to remove extra non-specific adsorbed aptamers. Then, 20 μL of 5 mM MCH solution

was dropped on the modified electrode for 1 h incubation at room temperature, in order to form a MCH film blocking the non-specific sites and obtain a well-aligned DNA monolayer (Tang et al., 2009; Wang et al., 2013a). Afterwards the prepared electrode was slowly rinsed with washing buffer solution and stored in dark at 4 °C for further usage.

2.4. Detection of DZN with the aptasensor

To detect target DZN molecules, the PEC aptasensor was incubated with different concentration (0.01, 0.1, 1, 10, 100, 1000, 10000 nM) of DZN in binding buffer solution at 60 °C in a thermostat for 1 h, and then rinsed with washing buffer solution. Finally, the PEC signals of DZN/MCH/aptamer/S-BN/Au/CN/FTO were measured in binding buffer solution (pH 7.4) at room temperature.

2.5. Real sample preparation

The PEC aptasensor was used for the determination of DZN in river water, tap water and apple samples where the pretreatment processes were accomplished as follows. Specifically, the apple samples were purchased from local markets, the tap water was obtained from local municipal pipelines, and the river water was collected from Xiangjiang River in Changsha, China. Firstly, 100 g of apple samples were ground by a mortar to obtain supernatant. Afterwards, both the supernatant and two water samples were treated through a filter membrane (0.22 μm) to filter suspended substances. At last, three different concentrations of DZN (10, 100, 1000 nM) were dropped on the obtained solution respectively by the standard addition method, and pH was adjusted to 7.4 by binding buffer solution before detection. To confirm the practical application ability of the aptasensor in different real samples, the results were compared with the high performance liquid chromatography-tandem mass spectrometry (HPLC-MS/MS) measurements.

3. Results and discussion

3.1. Characterization of the photoactive materials

The transmission electron microscopy (TEM) images of porous h-BN, S-BN, S-BN/CN and S-BN/Au/CN composites were shown to characterize the morphologies and structures. As shown in Fig. 1A, h-BN is in a typical sheet-like stacking structure with lots of randomly distributed mesopores whose interlayer distances was calculated to be 0.364 nm (Fig. S1B). The abundant pores might be ascribed to the released gas (like NH_3 and N_2) during material preparation process. Although after doping with S, the interlayer distances of S-BN became narrower with a size of 0.345 nm (Fig. S1C), Fig. S1A shows that S-BN owned the same microstructure with pure h-BN, demonstrating that the doping S didn't destroy the porous structure. And as shown in Fig. 1B, after the in-situ growth of layered CN on the surface of S-BN nanosheet, the obtained S-BN/CN became relatively rough and thick with the well preserved pore structures. Fig. 1C further reveals the successful synthesis of S-BN/Au/CN where numerous AuNPs with a diameter of 10–20 nm were well-dispersed on the surface. According to the related literature, the enhanced photocurrent density upon SPR excitation with a diameter of 10–20 nm was higher than the photocurrent of other sizes (Wang et al., 2017). Furthermore, a typical crystal spacing of 0.235 nm belonging to the (111) lattice plane of AuNPs could be observed clearly (see Fig. S1D). Additionally, the EDS mapping in Fig. 1D reveals the uniform distribution of all elements (B, C, N, O, S) in S-BN/Au/CN.

To further investigate the porous structure, the N_2 adsorption-desorption isotherms (Fig. S2) of h-BN, S-BN/CN, S-BN/Au/CN were measured. All the samples presented a type-IV isotherm with a H3 type hysteresis loop where the similar mesopore distribution illustrates the existence of highly porous structure (inset in Fig. S2). In addition, the corresponding BET specific surface areas and pore volumes are exhibited in Table S2, demonstrating that both the CN growth and AuNPs loading only gently reduced the BET surface areas and pore volumes, which was consist with the TEM results. Hence, the relatively large specific surface areas of prepared S-BN/Au/CN (200.408 m^2/g) could still endow it with substantial active reaction sites.

The X-ray diffraction (XRD) patterns were employed to analyze the crystalline phases of materials. As shown in Fig. 2A, the two main peak around 25.8° and 42.5° of h-BN sample are attributed to the (002) crystal planes and (100) crystal planes, corresponding to the interlayer stacking and in-plane packing of h-BN, respectively (Wang et al., 2013a). It is obvious that the (002) peak of S-BN shifts from 25.8° to 26.5°, indicating that doping S could lead to compacting the interlayer distances by the formation of new chemical bonds, which is consistent with the HR-TEM images (Figs. S1A and S1C). With the loading of CN, the S-BN/CN appears two (100) peaks corresponding to S-BN and CN, respectively, while the (002) peak exhibits a significant shift due to the formation of new interfacial phases (He et al., 2017). Comparing with binary composite, the four additional characteristic peaks of S-BN/Au/CN located at 38.2°, 44.5°, 64.4° and 77.5° correspond to (111), (200), (220) and (311) crystal planes of Au, respectively, on the grounds of the standard value (JCPDS card 04–0784), indicating the successful deposition of gold nanoparticles (Peng et al., 2018).

The X-ray photoelectron spectroscopy (XPS) was used to further confirm the element chemical states of the prepared materials (Yu et al., 2019). Fig. 2B indicates the main characteristic peaks of B 1s, C 1s, N 1s, O 1s and Au 4f, while the peak of S element is not obvious which might be due to its low concentration. Furthermore, the high resolution spectra of individual elements were also analyzed respectively. In Fig. 2C, the high-resolution spectra of S 2p proves the successfully doping of S element where the peak at 163.74 eV corresponds to the formation of new chemical bond. Additionally, two binding energy values located around 84.80 eV and 88.51 eV of Au 4f (Fig. 2D) correspond to Au 4f 7/2 and Au 4f 5/2, well suggesting the successful load of AuNPs on the composite (Li et al., 2015a). Meanwhile, as for the B 1s spectrum (Fig. S3A), the binding energy value of 190.70 eV is attributed to the B–N bonds, and the characteristic peak around 192.20 eV reveals a primary B–O bonds (Jiang et al., 2018). The N 1s XPS spectrum is presented in Fig. S3B, where the peak at 398.20 eV belongs to the N–B bond, and the shoulder peak located at 398.96 eV and 400.20 eV are assigned to C–N–B and C–N=C, respectively (Huang et al., 2014; Wang et al., 2016), which further reveals the CN in-situ growth on the surface of S-BN. Moreover, the main peak in C 1s spectra (Fig. S3C) at 288.40 eV is assigned to the N–C=N bonds, while the subordinate peak at 284.64 eV is ascribed to the adventitious carbon species (Dong et al., 2013; Xu et al., 2013).

The ultraviolet visible diffuse reflectance spectra (UV–vis DRS) was shown to identify the electronic structures and optical properties. As depicted in Fig. 3A, the absorption edge of S-BN shows a remarkable red shift with S-doped, inferring the decrease of bandgap. Furthermore, the absorbance and absorption range of S-BN/Au/CN have an enormously co-enhancement due to the load of CN and the SPR effect of AuNPs. To investigate the electronic band structure in detail, the band gap of CN, h-BN and S-BN were calculated by the Kubelk-Munk method according to the formula as follows (Deng et al., 2016):

$$\alpha hv = A(hv - E_g)^{n/2} \quad (1)$$

where α, h, v, A and E_g represent the absorption coefficient, Planck constant, light frequency, a constant and band gap energy, respectively. The n values of h-BN and g-C_3N_4 are 1 which depend on properties of semiconductors (Xia et al., 2017; Zhang et al., 2018). As shown in Tauc's plots (Fig. 3B), the bandgap of pure h-BN is about 3.78eV, and as expected S-BN presents a reduced bandgap of 2.96 eV corresponding to our previous inference. Simultaneously, CN owns a bandgap of 2.72 eV, which is similar to the reports in the literature (Jiang et al., 2017).

The cyclic voltammetry (CV) curve was used to further investigate

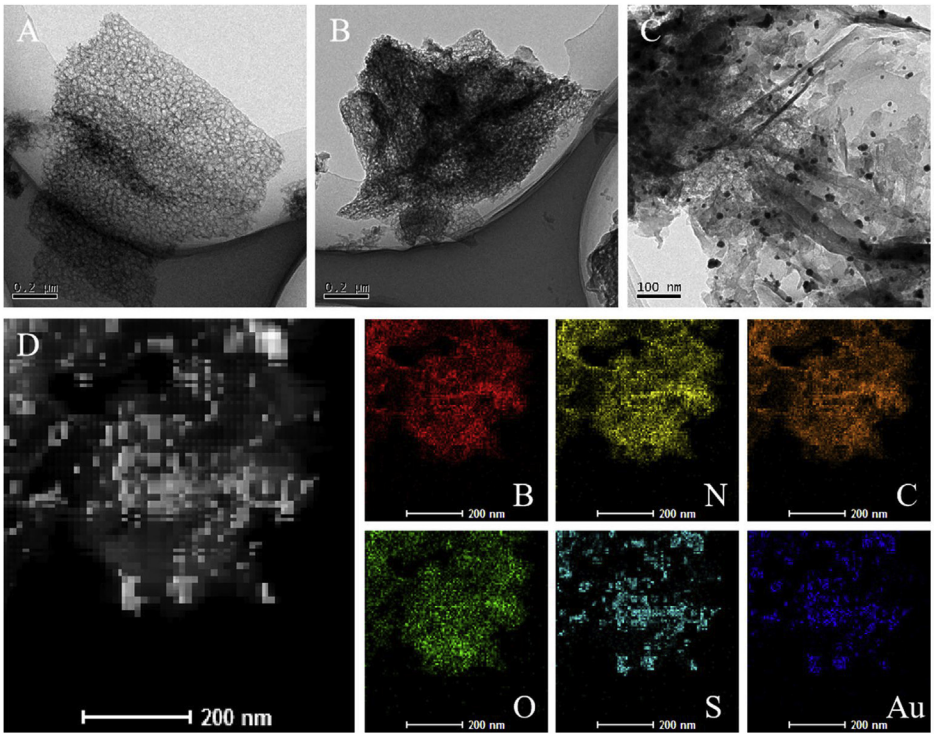

Fig. 1. TEM images of (A) pure h-BN, (B) S-BN/CN and (C) S-BN/Au/CN; (D) HAADF-STEM image and EDS mapping of S-BN/Au/CN.

the conduction band (CB) and valence band (VB) of photoactive semiconductors according to the formula as follows (Wang et al., 2019):

$$E_{VB} = -(4.8 + E_{oxidation} - E_{1/2}^{Fc/Fc+}) \quad (2)$$

$$E_{CB} = E_{VB} + E_g \quad (3)$$

where $E_{oxidation}$ is the oxidation initiation potential, and $E_{1/2}^{Fc/Fc+}$ is the formal potential of the ferrocene/ferrocenium (Fc/Fc^+) couple. Potentials were calibrated with Fc/Fc^+, and the potential of Fc/Fc^+ had an absolute energy level of 4.80 eV to vacuum. As shown in Fig. 3C, the $E_{oxidation}$ of S-BN and CN are 2.62 and 1.5 V, respectively. The $E_{oxidation}$ of h-BN and $E_{1/2}^{Fc/Fc+}$ are estimated to 2.62 and 0.48 V according to the tangents of oxidation peaks (Fig. S4). Thus, the E_{VB} of −6.94, −5.82 and −6.94 eV could be determined for S-BN, CN and h-BN. Consequently, the E_{CB} of S-BN, CN and h-BN were calculated to −3.98, −3.10 and −3.06 eV, respectively. On the basis of the calculation results, it could be inferred that S doping didn't change E_{VB} of h-BN, but reduced the E_{CB}. These values were significant for the electron-hole transfer pathway of the S-BN/Au/CN photoactive material.

The photoluminescence (PL) spectra was used to characterize the migration and recombination of photogenerated carriers (Tang et al., 2016). All the samples were measured under an excitation wavelength of 350 nm. As shown in Fig. 3D, the pure CN suggests a strong emission peak, while the peak intensity of S-BN/CN has a sharp decline, revealing that the composites possess a low recombination rate of electron-hole pairs. Moreover, the peak intensity of S-BN/Au/CN was further reduced owing to AuNPs as the electron-hole pairs recombination centers, capturing electrons from CB of S-BN and holes from VB of CN to extremely decrease the recombination of photogenerated carriers. As expected, pure h-BN and S-BN can hardly be excited under visible-light irradiation (inset in Fig. 3D) because of the wide bandgap (Golberg et al., 2010). Meanwhile, the doped S gave rise to a great reduction of emission peak, illustrating that it could facilitate the separation of photogenerated electrons and holes.

3.2. Photoelectrochemical characterization of the fabricated PEC aptasensor

Electrochemical impedance spectroscopy (EIS) was used to monitor the processes of interfacial charge transfer (Fig. 4A). Typically, the semicircle diameter in Nyquist plot represents the electron-transfer resistance (R_{ct}; Ω) value, which dominated the electron transfer kinetics of redox probe at the electrode interface (Tang et al., 2009). All the measurements were conducted in binding buffer solution containing 5 mM $[Fe(CN)_6]^{3-/4-}$ with 20 mM KCl (PH 7.4). Obviously, the smallest semicircle diameter (curve a) was ascribed to the bare FTO electrode, while the resistance of h-BN modified FTO exhibited a sharp increased (curve b), indicating that the pure h-BN had a serious conductivity due to its wide bandgap. The semicircle diameter of S-BN/FTO (curve c) decreased due to the reduced bandgap by S doping. Meanwhile, the R_{ct} of S-BN/CN/FTO (curve d) had a tremendous reduction, suggesting that the formation of S-BN/CN heterojunction could generate built-in electric field at the contact interface of S-BN and CN, which could promote the migration of electrons and reduce resistance. Furthermore, the deposition of AuNPs further decreased the resistance (curve e) because it could facilitate the charge transfer process at the electrode surface. When aptamers were dropped on the surface of prepared materials, the resistance value increased dramatically (curve f) due to the repulsion force between aptamers with negative charges and the negatively charged $[Fe(CN)_6]^{3-/4-}$ species, which inhibited the electron transfer. With the addition of MCH (curve g), the active sites were blocked, resulting in the increased of R_{ct}. After the prepared electrode was incubated in 1 nM DZN solution (curve h), its resistance value was further raised. It could be interpreted that the aptamers on the surface of electrode had a specific reaction with DZN molecules and formed abundant aptamer-DZN complexes, which increased the steric hindrance effect of the electron transfer between electrode and $[Fe(CN)_6]^{3-/4-}$ solution. Additionally, the equivalent circuit (inset in Fig. 4A) including charge transfer resistance (R_{ct}), warburg impedance (Z_w), solution resistance (R_s), and interfacial capacitance (C_{dl}), as well as the parameters in detail are presented in Table S3. All of the above phenomena revealed that S-BN/Au/CN was successfully immobilized

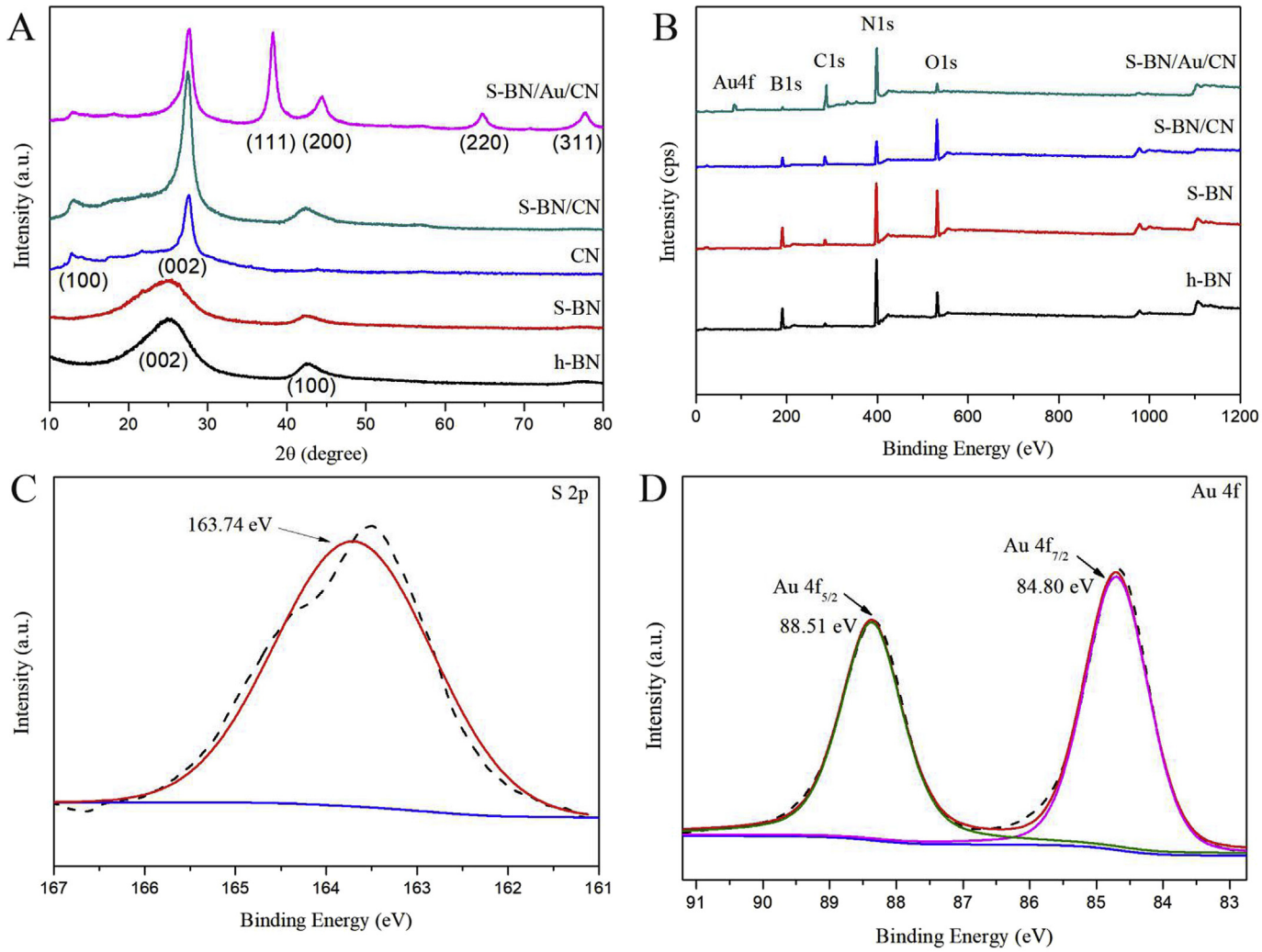

Fig. 2. (A) XRD patterns of h-BN, S-BN, CN, S-BN/CN and S-BN/Au/CN; (B) The full-scale XPS spectra of h-BN, S-BN, S-BN/CN, S-BN/Au/CN and high-resolution XPS spectra of S-BN/Au/CN: (C) S 2p, (D) Au 4f.

on the FTO electrode.

Subsequently, the modified electrodes were measured for photocurrent responses in binding buffer solution without applied potential under intermittent visible-light irradiation. As can be seen in Fig. 4B, the weakest photocurrent signal of h-BN/FTO (curve a) was due to the wide bandgap and high recombination rate of electron-hole pairs. The photocurrent responses of S-BN/FTO (curve b) had a sharp increase as the introduction of S narrowed down the bandgap. In contrast, ascribed to the efficient separation of photogenerated charge carriers and low recombination rate of electron-hole pairs, S-BN/CN/FTO composite produced a higher photocurrent response (curve c). Furthermore, the electrode modified with S-BN/Au/CN/FTO (curve d) produced the strongest photocurrent intensity, which might be ascribed to the enhanced absorption efficiency of visible-light irradiation by the SPR effect of AuNPs. However, when the aptamer (curve e) and MCH (curve f) were immobilized on S-BN/Au/CN/FTO modified electrode, the photocurrent signals were obviously decreased owing to the hindered electron transfer corresponding to the EIS results. At last, the prepared aptasensor was incubated in 1 nM DZN, where a significant decline of the anodic photocurrent signal could be observed (curve g). It could be explained that the formation of aptamer-DZN increased the steric hindrance and inhibited the transfer of electrons. These analyses of photocurrent signals were in accordance with the EIS results, demonstrating that the PEC aptasensor was successfully established for detection of DZN on the basis of S-BN/Au/CN.

3.3. Mechanism study and verification

The mechanism of photocurrent generation and DZN detection is exhibited in Scheme 1. Presumably, if pure h-BN and CN constructed the heterojunction, the photogenerated electrons from the CB of h-BN should flow into the CB of CN, and the photogenerated holes from the VB of h-BN might transfer to the VB of CN. But obviously, this heterojunction was unsatisfactory because of its instability and high recombination rate of electron-hole pairs. As for the construction of h-BN based Z-scheme heterojunction of S-BN/Au/CN, CN was easily excited and S-BN could also be excited due to the reduced bandgap by doping S under visible-light irradiation, where abundant photogenerated electrons and holes were produced in the CB and VB, respectively. Notably, doping S only changed the CB of h-BN, and the VB position was almost constant corresponding to the calculations above. After deposition of AuNPs, a new Z-scheme charge transfer was constructed. Exactly both the photogenerated electrons in CB of S-BN and the photogenerated holes in VB of CN transferred to the AuNPs due to the formation of new recombination centers, which inhibited the recombination of electron-hole pairs. Simultaneously, AuNPs promoted the utilization of visible light attributed to the SPR effect, which facilitated the separation of photogenerated charge carriers. Therefore, the h-BN based photoactive material exhibited an extremely high photocurrent signal due to the synergistic effect as above mentioned. With the presence of DZN, the formation of aptamer-DZN complexes brought about the photocurrent

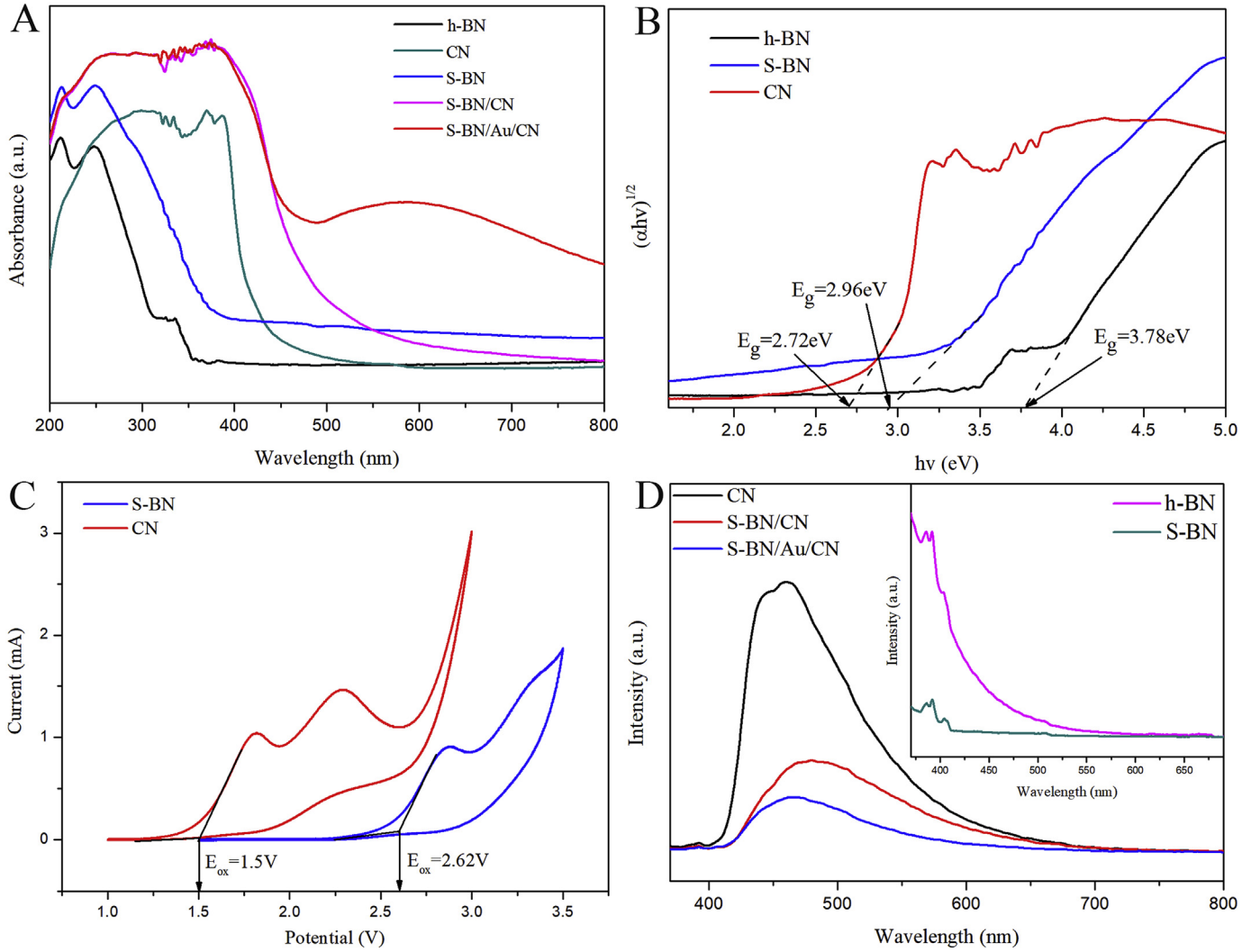

Fig. 3. (A) UV–vis diffuse reflectance spectra of h-BN, S-BN, CN, S-BN/CN and S-BN/Au/CN; (B) Tauc's plots of $(\alpha hv)^{1/2}$ vs. photon energy (hv) and (C) CVs of the FTO modified by S-BN and CN in a deoxygenated anhydrous acetonitrile solution of tetrabutylammonium hexafluorophosphate (0.1 M) at scan rate of 50 mV/s, a Ag/AgCl reference electrode (with saturated KCl), with a Pt wire counter electrode; (D) The PL spectra of CN, S-BN/CN, S-BN/Au/CN and h-BN, S-BN (inset).

significantly decreased on account of the steric hindrance effect with the inhibited transfer of charges. Consequently, the novel h-BN based self-powdered PEC aptasensor could realize ultrasensitive detection of diazinon with excellent photoelectric conversion efficiency.

The charge transfer mechanism was expounded and verified by the electron spin resonance (ESR) spin-trap technique with the signals of superoxide ($\bullet O_2^-$) and hydroxyl (•OH) radicals. These radical detection experiments of S-BN, S-BN/CN, and S-BN/Au/CN were carried out under dark conditions, and visible-light irradiation of 5 min, and 10 min, respectively. As shown in Fig. 4C and D, the characteristic signals of DMPO-•OH of S-BN could be observed, while DMPO-O_2^- of S-BN couldn't be observed, which might be caused by the fact that the lowered CB by doping S could not reach the standard redox potentials to reduce O_2 to $\bullet O_2^-$ (Zhang et al., 2014). With the in-situ growth of CN, both $\bullet O_2^-$ and •OH radicals of S-BN/CN were produced, illustrating that the electrons of S-BN/CN accumulated on the CB of CN and the holes accumulated on the VB of S-BN, which could further verify the construction of Z-scheme heterojunction instead of type II heterojunction in S-BN/CN. Moreover, the two DMPO- signals of S-BN/Au/CN had a simultaneous enhancement, which revealed that the loading of AuNPs boosted the generation of radicals. The related reaction route of S-BN/Au/CN was exhibited as follows:

$$\text{S-BN/Au/CN} + hv \rightarrow \text{S-BN/Au/CN}\ (e^- + h^+) \quad (4)$$

$$e^- + O_2 \rightarrow \bullet O_2^- \quad (5)$$

$$h^+ + H_2O \rightarrow \bullet OH + H^+ \quad (6)$$

Therefore, the novel h-BN based Z-scheme heterojunction was constructed successfully and could produce abundant superoxide and hydroxyl radicals.

3.4. Optimization of experiment conditions for the PEC aptasensor

In order to enhance the performance of the PEC aptasensor in every step, some relevant experimental parameters were optimized, where the mass ratios of melamine, the weight ratios of AuNPs, aptamer concentration, pH of binding buffer solution, and incubation time of the DZN were all contained. The concentration of DZN is 100 nM in the experimental optimization processes. Fig. S5A reveals that the photocurrent of S-BN/CN/FTO electrode increased initially and then declined with the mass ratios of melamine to S-BN increasing from 5 to 25, suggesting that the appropriate loading of CN could enhance the PEC activity of S-BN/CN. As shown in Fig. S5B, with the load of AuNPs, the photocurrent gradually increased due to the SPR effect and reached the maximum value at 5% AuNPs load, while excessive AuNPs may block surface active sites and lower the absorption efficiency of visible-light

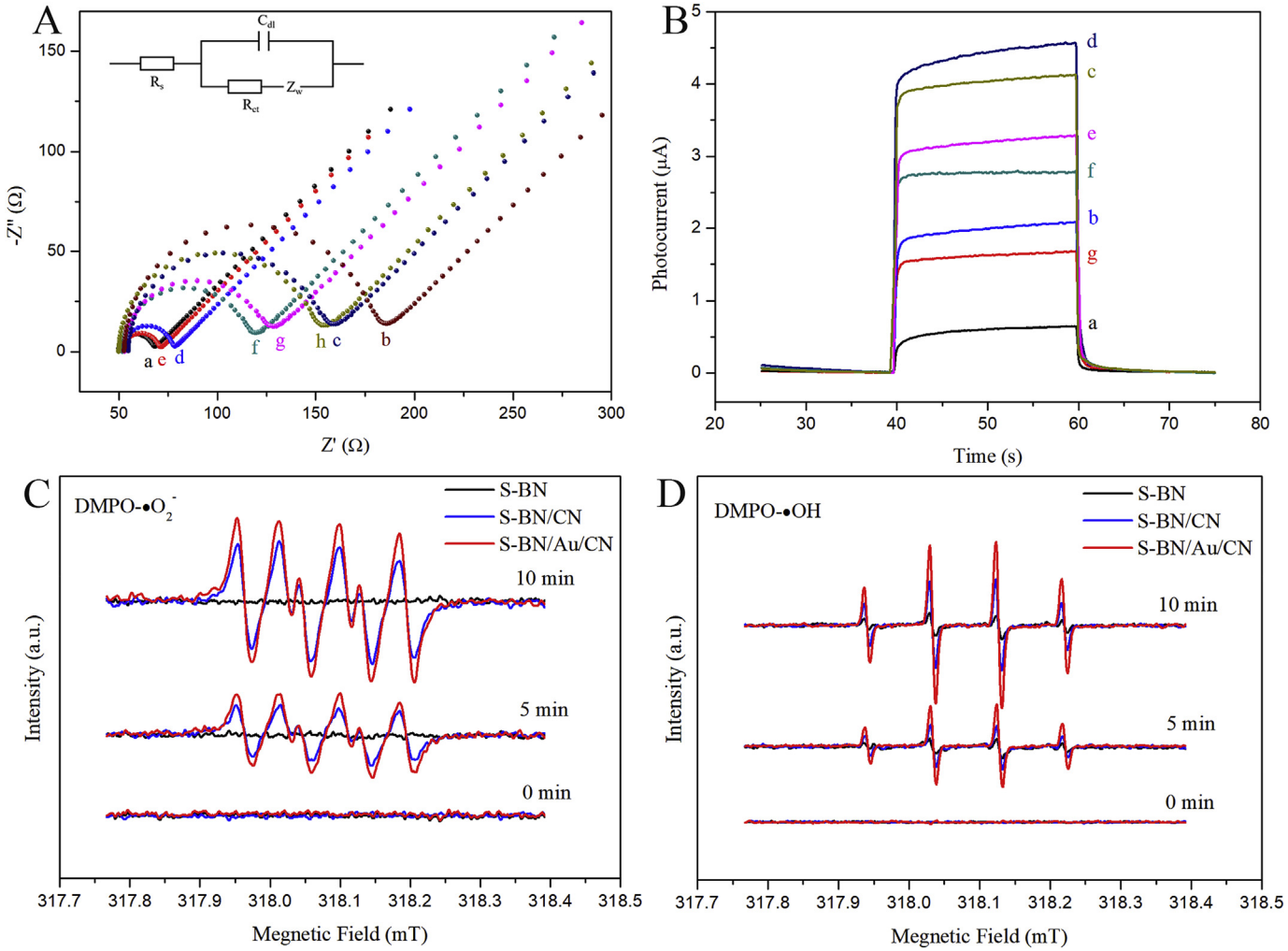

Fig. 4. (A) Electrochemical impedance spectra of (a) FTO electrode, (b) h-BN/FTO, (c) S-BN/FTO, (d) S-BN/CN/FTO, (e) S-BN/Au/CN/FTO, (f) aptamer/S-BN/Au/CN/FTO, (g) MCH/aptamer/S-BN/Au/CN/FTO (h) MCH/aptamer/S-BN/Au/CN/FTO incubated with 1 nM DZN in binding buffer solution containing 5 mM $[Fe(CN)_6]^{3-/4-}$ with 20 mM KCl (PH 7.4); (B) Photocurrent responses of (a) h-BN/FTO, (b) S-BN/FTO, (c) S-BN/CN/FTO (d) S-BN/Au/CN/FTO, (e) aptamer/S-BN/Au/CN/FTO, (f) MCH/aptamer/S-BN/CN/FTO, (g) MCH/aptamer/S-BN/Au/CN/FTO incubated with 1 nM DZN in binding buffer solution without applied potential; DMPO spin-trapping ESR spectra of (C) DMPO-•O_2^- (D) DMPO-•OH with S-BN, S-BN/CN, S-BN/Au/CN at 0 min, 5 min and 10 min under visible-light irradiation.

irradiation. As demonstrated in Fig. S5C, with the increased concentration of aptamer, the photocurrent decreased and then remained stable. It could be explained that the decrease of photocurrent was attributed to the impeded charges transfer of aptamer and stable photocurrent might be due to the saturated Au–S bonds between AuNPs and aptamer. The pH value of binding buffer solution was also optimized (Fig. S5D), the photocurrent intensity reached the lowest at pH 7.4 because the aptamer was easily inactivated in the overly acidic or alkaline environment. Additionally, Fig. S5E illustrated that the photocurrent intensity declined piece by piece when the incubation time increased from 20 to 60 min, and kept stable with the time increase. It could be explained that long incubation time might promote the formation of aptamer-DZN complexes until the binding reaction reached saturation. Therefore, the optimized CN, AuNPs weight ratios (5%), aptamer concentration (2.5 μM), pH (7.4), incubation time (60 min) were chosen in all experiments, unless otherwise mentioned.

3.5. Performance of the PEC aptasensor

Under the optimal conditions above, the photocurrent response was measured by the fabricated PEC aptasensor at a series of DZN concentration in binding buffer solution. As shown in Fig. 5A, the anodic photocurrent gradually reduced with the concentration of DZN varied from 0.01 to 10000 nM due to the steric hindrance effect. The linear regression equation (Fig. 5B) was $\Delta I = 0.322 \lg C_{DZN} + 0.778$ ($R^2 = 0.996$), where ΔI is the difference value between the photocurrent of MCH/aptamer/S-BN/Au/CN and DZN/MCH/aptamer/S-BN/Au/CN. The limit of detection (LOD) was calculated according to formula 3σ/s (the method details are available in the "Supporting Information" file) (Çakıroğlu and Özacar, 2018). Therefore, the calculated LOD of this aptasensor for DZN detection was 6.8 pM. Compared with previously reported methods for DZN detection (Table S4), the proposed PEC aptasensor displayed excellent performance with relatively wider linear range and lower detection limit.

3.6. Selectivity, reproducibility and stability of the PEC aptasensor

The selectivity of the fabricated PEC aptasensor was measured by interference experiment with 100 nM DZN and other representative interfering species including phorate, malathion, profenofos and deltamethrin of same concentration. As shown in Fig. 5C, compared with blank group, the photocurrent signals of four other pesticides were unchanged. However, the photocurrent intensity of DZN obviously decreased, which was almost identical to photocurrent value of the mixture (consist of all pesticides above). These phenomena could be explained that the high selectivity between the proposed aptasensor

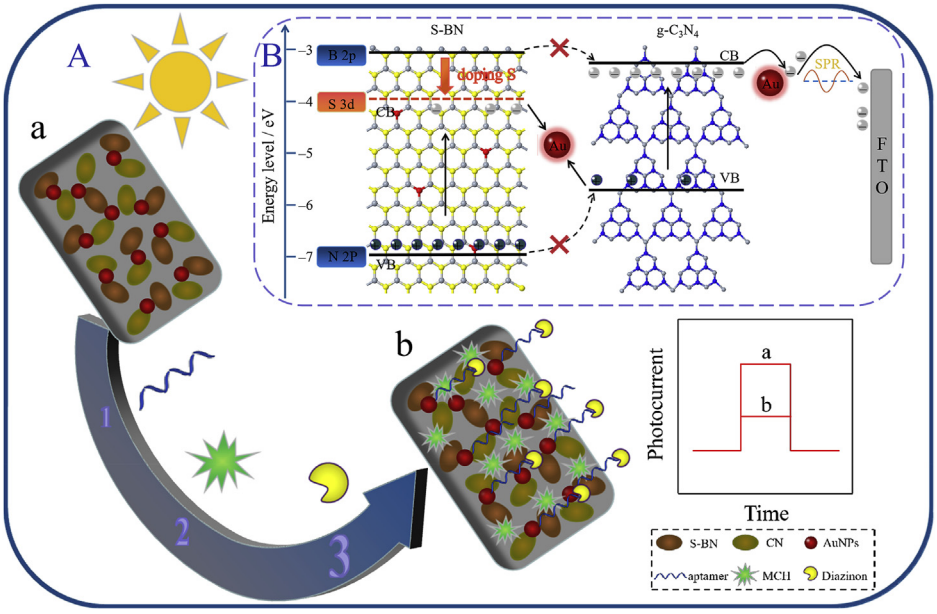

Scheme 1. Schematic illustration of (A) h-BN based PEC aptasensor for DZN detection, and (B) enhanced photoelectric conversion efficiency process for S-BN/Au/CN.

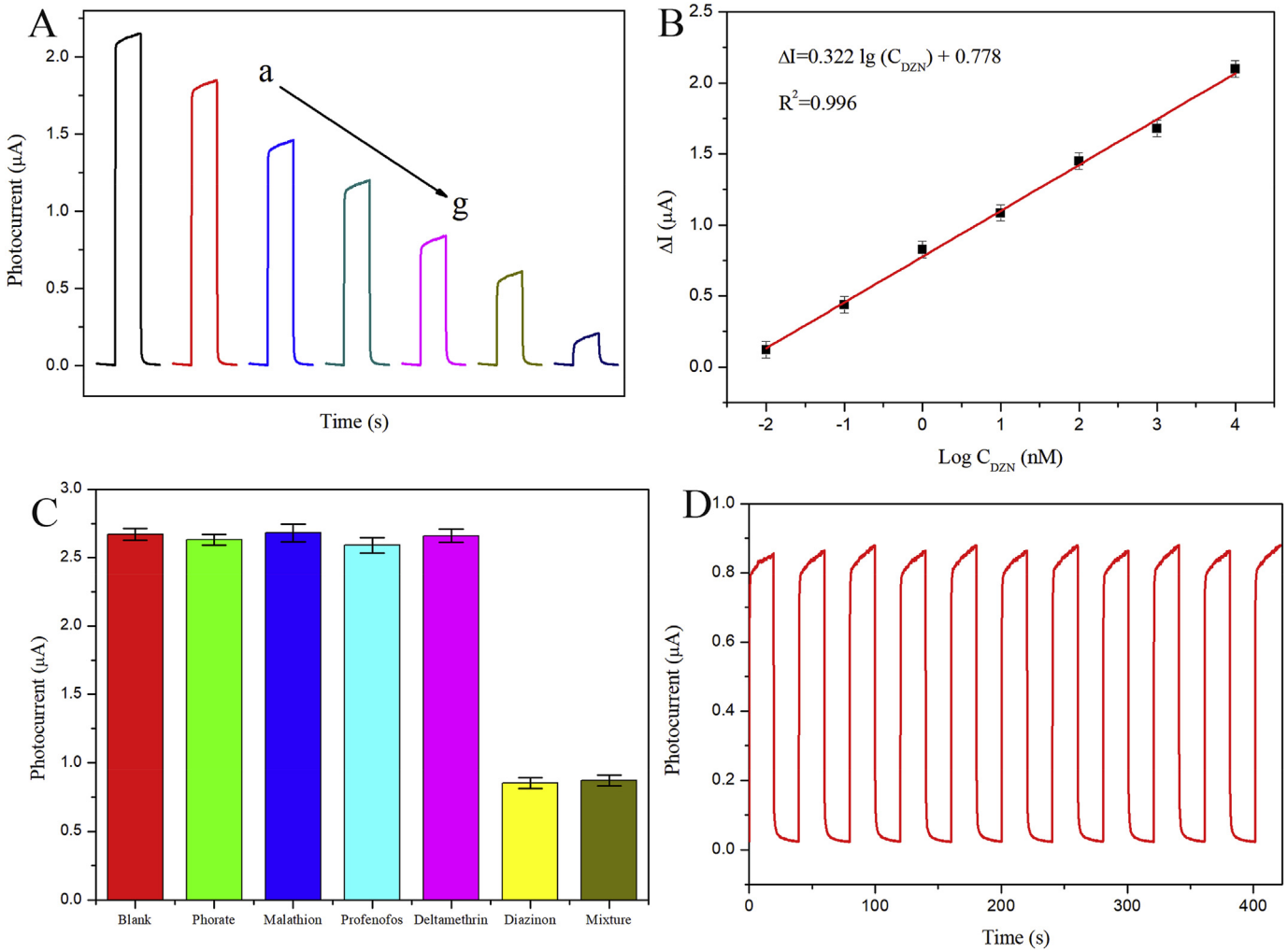

Fig. 5. (A) Photocurrent responses of the aptasensor at different concentrations of DZN (from a to g: 0.01, 0.1, 1, 10, 100, 1000, 10000 nM) in binding buffer solution; (B) The corresponding linear regression equation; (C) Selectivity for the fabricated PEC aptasensor: blank, phorate, malathion, profenofos, deltamethrin, diazinon and the mixture (consist of all pesticides above) with same concentration; (D) Stability for the proposed PEC aptasensor incubated with 100 nM DZN.

and DZN molecules, and the interference of other pesticides was ignorable.

To confirm the reproducibility of the aptasensor, five independent MCH/aptamer/S-BN/Au/CN modified FTO electrodes were incubated with 100 nM DZN at the same conditions. The relative standard deviation (RSD) was calculated to be 3.73%, which illustrated the good reproducibility of the prepared PEC aptasensor.

Furthermore, the photocurrent signal of aptasensor detection for 100 nM DZN, was carried out under 10 on-off cycles to characterize the stability. As demonstrated in Fig. 5D, after 400 s, the photocurrent intensity had no noticeable variation and maintained 98.8% of normal value, revealing the excellent stability of the proposed PEC aptasensor. After stored at 4 ˚C for 1 month, the photocurrent signal still remained 96.7% of the original value, revealed excellent long-term stability of the self-powered PEC aptasensor.

3.7. Real samples analysis

The practical application capability of the fabricated PEC aptasensor was verified in three different real samples. In addition, these samples solution were prepared in detail according to the procedure of Section 2.4. As shown in Table S5, the recoveries of the samples solution were in the range of 98.03%–102.21% with a RSD value in the range of 3.58–5.72%, which is essentially consistent with the results acquired by HPLC-MS/MS. Thus, all results demonstrated that the proposed PEC aptasensor possessed the enormous potential applicability in different environment conditions.

4. Conclusion

In this work, a self-powered PEC aptasensor was successfully fabricated for ultrasensitive detection of DZN based on a novel h-BN based photoactive material with extremely high efficiency of photoelectric signal conversion. The construction of h-BN based photoactive material by S doping and coupling with CN, which promoted the absorption of visible light, improved the separation of photogenerated carriers and inhibited the recombination of electron-hole pairs. In addition, the loaded AuNPs further enhanced the photoelectric performances due to SPR effect and the formation of new electron-hole pairs recombination centers. Furthermore, the proposed PEC aptasensor for DZN detection presented a linear range from 0.01 to 10000 nM and a detection limit of 6.8 pM with high selectivity, good reproducibility and excellent stability, and exhibited a great application in three different environmental real samples. In summary, this work proved that it is feasible to apply PEC aptasensor in the detection of DZN and other OP pesticides. Moreover, it is believed that our designing ideas of the h-BN based material will provide a bright prospect of various innovative photoactive materials for universal PEC bioanalysis. In the future work, the density functional theory (DFT) calculations may be applied to investigate the energy band structure and electron transfer, and to develop more photoactive materials with excellent performance for PEC biosensor.

Declaration of interest statement

No conflict of interest exits in the submission of this manuscript, and the manuscript is approved by all the authors for publication. We would like to declare that this work described is original research that has not been published previously, and not under consideration for publication elsewhere, in whole or in part.

CRediT authorship contribution statement

Jisui Tan: Writing - original draft. **Bo Peng:** Investigation. **Lin Tang:** Writing - review & editing. **Chengyang Feng:** Investigation. **Jiajia Wang:** Data curation. **Jiangfang Yu:** Data curation. **Xilian Ouyang:** Formal analysis. **Xu Zhu:** Formal analysis.

Acknowledgements

The study was supported by Projects 51579096, 51521006 and 51222805 supported by National Natural Science Foundation of China, the Key Research and Development Program of Hunan Province of China (2017SK2241), the National Innovative Talent Promotion Program of China (2017RA2088), the Funds for Innovative Province Construction of Hunan Province of China (2019RS3012), the National Program for Support of Top-North Young Professionals of China (2012).

Appendix A. Supplementary data

Supplementary data to this article can be found online at https://doi.org/10.1016/j.bios.2019.111546.

References

Armstrong, J.L., Dills, R.L., Yu, J., Yost, M.G., Fenske, R.A., 2014. J. Environ. Sci. Health Part B 49, 102–108.
Bhattacharjee, S., Fakhruddin, A.N.M., Chowdhury, M.A.Z., Rahman, M.A., Alam, M.K., 2012. Environ. Contam. Toxicol. 89, 348–353.
Çakıroğlu, B., Özacar, M., 2018. Biosens. Bioelectron. 119, 34–41.
Dai, W.-X., Zhang, L., Zhao, W.-W., Yu, X.-D., Xu, J.-J., Chen, H.-Y., 2017. Anal. Chem. 89, 8070–8078.
Deepak, F., Vinod, C., Mukhopadhyay, K., Govindaraj, A., Rao, C., 2002. Chem. Phys. Lett. 353, 345–352.
Deng, Y., Tang, L., Feng, C., Zeng, G., Wang, J., Zhou, Y., Liu, Y., Peng, B., Feng, H., 2018. J. Hazard Mater. 344, 758–769.
Deng, Y., Tang, L., Zeng, G., Wang, J., Zhou, Y., Wang, J., Tang, J., Liu, Y., Peng, B., Chen, F., 2016. J. Mol. Catal. A Chem. 421, 209–221.
Di, J., Xia, J., Ji, M., Wang, B., Yin, S., Zhang, Q., Chen, Z., Li, H., 2016. Appl. Catal., B 183, 254–262.
Dong, F., Zhao, Z., Xiong, T., Ni, Z., Zhang, W., Sun, Y., Ho, W.-K., 2013. ACS Appl. Mater. Interfaces 5, 11392–11401.
Golberg, D., Bando, Y., Huang, Y., Terao, T., Mitome, M., Tang, C., Zhi, C., 2010. ACS Nano 4, 2979–2993.
Hassani, S., Akmal, M.R., Salek-Maghsoudi, A., Rahmani, S., Ganjali, M.R., Norouzi, P., Abdollahi, M., 2018. Biosens. Bioelectron. 120, 122–128.
Hattori, Y., Taniguchi, T., Watanabe, K., Nagashio, K., 2014. ACS Nano 9, 916–921.
He, F., Chen, G., Yu, Y., Zhou, Y., Zheng, Y., Hao, S., 2015. Chem. Commun. 51, 425–427.
He, Z., Kim, C., Lin, L., Jeon, T.H., Lin, S., Wang, X., Choi, W., 2017. Nano Energy 42, 58–68.
Hu, T., Zheng, Y.-N., Li, M.-J., Liang, W.-B., Chai, Y.-Q., Yuan, R., 2018. Anal. Chem. 90, 6096–6101.
Huang, C., Ye, W., Liu, Q., Qiu, X., 2014. ACS Appl. Mater. Interfaces 6, 14469–14476.
Huang, Y., Fan, W., Long, B., Li, H., Zhao, F., Liu, Z., Tong, Y., Ji, H., 2016. Appl. Catal., B 185, 68–76.
Jenkins, A.L., Yin, R., Jensen, J.L., 2001. Analyst 126, 798–802.
Jiang, L., Yuan, X., Pan, Y., Liang, J., Zeng, G., Wu, Z., Wang, H., 2017. Appl. Catal., B 217, 388–406.
Jiang, L., Yuan, X., Zeng, G., Wu, Z., Liang, J., Chen, X., Leng, L., Wang, H., Wang, H., 2018. Appl. Catal., B 221, 715–725.
Kang, Z., Gu, Y., Yan, X., Bai, Z., Liu, Y., Liu, S., Zhang, X., Zhang, Z., Zhang, X., Zhang, Y., 2015a. Biosens. Bioelectron. 64, 499–504.
Kang, Z., Yan, X., Wang, Y., Bai, Z., Liu, Y., Zhang, Z., Lin, P., Zhang, X., Yuan, H., Zhang, X., 2015b. Sci. Rep. 5, 7882.
Lei, W., Portehault, D., Liu, D., Qin, S., Chen, Y., 2016. Nat. Commun. 4, 1777.
Li, J., Han, M., Guo, Y., Wang, F., Sun, C., 2016. Chem. Eng. J. 298, 300–308.
Li, M.-J., Zheng, Y.-N., Liang, W.-B., Yuan, R., Chai, Y.-Q., 2017. ACS Appl. Mater. Interfaces 9, 42111–42120.
Li, W., Feng, C., Dai, S., Yue, J., Hua, F., Hou, H., 2015a. Appl. Catal., B 168, 465–471.
Li, W., Wang, Q., Huang, L., Li, Y., Xu, Y., Song, Y., Zhang, Q., Xu, H., Li, H., 2015b. RSC Adv. 5, 88832–88840.
Liu, G., Niu, P., Sun, C., Smith, S.C., Chen, Z., Lu, G.Q., Cheng, H.M., 2010. J. Am. Chem. Soc. 132, 11642–11648.
Pakdel, A., Bando, Y., Golberg, D., 2014. Chem. Soc. Rev. 43, 934–959.
Peng, B., Tang, L., Zeng, G., Fang, S., Ouyang, X., Long, B., Zhou, Y., Deng, Y., Liu, Y., Wang, J., 2018. Biosens. Bioelectron. 121, 19–26.
Shang, M., Zhang, J., Qi, H., Gao, Y., Yan, J., Song, W., 2019. Biosens. Bioelectron. 136, 53–59.
Tang, L., Feng, C., Deng, Y., Zeng, G., Wang, J., Liu, Y., Feng, H., Wang, J., 2018a. Appl. Catal., B 230, 102–114.
Tang, L., Wang, J., Zeng, G., Liu, Y., Deng, Y., Zhou, Y., Tang, J., Wang, J., Guo, Z., 2016. J. Hazard Mater. 306, 295–304.
Tang, L., Yu, J., Pang, Y., Zeng, G., Deng, Y., Wang, J., Ren, X., Ye, S., Peng, B., Feng, H., 2018b. Chem. Eng. J. 336, 160–169.
Tang, L., Zeng, G., Shen, G., Li, Y., Liu, C., Li, Z., Luo, J., Fan, C., Yang, C., 2009. Biosens. Bioelectron. 24, 1474–1479.

Wang, C., Nie, X.G., Shi, Y., Zhou, Y., Chen, H.Y., 2017. ACS Nano 11, 5897–5905.
Wang, H.-H., Li, M.-J., Wang, H.-J., Chai, Y.-Q., Yuan, R., 2019. ACS Appl. Mater. Interfaces 11, 23765–23772.
Wang, H., Yuan, X., Wang, H., Chen, X., Wu, Z., Jiang, L., Xiong, W., Zeng, G., 2016. Appl. Catal., B 193, 36–46.
Wang, J., Kong, L., Guo, Z., Xu, J., Liu, J., 2010. J. Mater. Chem. 20, 5271–5279.
Wang, J., Tang, L., Zeng, G., Deng, Y., Dong, H., Liu, Y., Wang, L., Peng, B., Zhang, C., Chen, F., 2018. Appl. Catal., B 222, 115–123.
Wang, L., Ni, S.-Q., Guo, C., Qian, Y., 2013a. J. Mater. Chem. A 1, 6379–6387.
Wang, X., Qiao, X., Ma, Y., Zhao, T., Xu, Z., 2013b. J. Agric. Food Chem. 61, 3821–3827.
Watanabe, K., Taniguchi, T., Kanda, H., 2004. Nat. Mater. 3, 404–409.
Weng, Q., Ide, Y., Wang, X., Wang, X., Zhang, C., Jiang, X., Xue, Y., Dai, P., Komaguchi, K., Bando, Y., 2015. Nano Energy 16, 19–27.
Wu, J., Fu, X., Xie, C., Yang, M., Fang, W., Gao, S., 2011. Sens. Actuators, B 160, 511–516.
Xia, Y., Li, Q., Lv, K., Tang, D., Li, M., 2017. Appl. Catal., B 206, 344–352.
Xu, H., Liu, L., Song, Y., Huang, L., Li, Y., Chen, Z., Zhang, Q., Li, H., 2016. J. Alloy. Comp. 660, 48–54.
Xu, J., Zhang, L., Shi, R., Zhu, Y., 2013. J. Mater. Chem. A 1, 14766–14772.
Yu, J., Tang, L., Pang, Y., Zeng, G., Wang, J., Deng, Y., Liu, Y., Feng, H., Chen, S., Ren, X., 2019. Chem. Eng. J. 364, 146–159.
Zhang, J., Hu, Y., Jiang, X., Chen, S., Meng, S., Fu, X., 2014. J. Hazard Mater. 280, 713–722.
Zhang, Q., Chen, P., Zhuo, M., Wang, F., Su, Y., Chen, T., Yao, K., Cai, Z., Lv, W., Liu, G., 2018. Appl. Catal., B 221, 129–139.
Zhang, Y., Lee, H.K., 2013. J. Chromatogr. A 1271, 56–61.
Zhao, K., Yan, X., Gu, Y., Kang, Z., Bai, Z., Cao, S., Liu, Y., Zhang, X., Zhang, Y., 2016. Small 12, 245–251.
Zhao, W.-W., Xu, J.-J., Chen, H.-Y., 2014. Chem. Rev. 114, 7421–7441.
Zheng, Y., Liang, W., Yuan, Y., Xiong, C., Xie, S., Wang, H., Chai, Y., Yuan, R., 2016. Biosens. Bioelectron. 81, 423–430.
Zhou, P., Yu, J., Jaroniec, M., 2014. Adv. Mater. 26, 4920–4935.